Morphodynamic equilibrium in straight tidal channels: Combined effects of Coriolis force and external overtides

G. P. Schramkowski and H. E. de Swart

Institute for Marine and Atmospheric Research, Utrecht University, Utrecht, The Netherlands

Received 27 October 2000; revised 14 March 2002; accepted 16 April 2002; published 24 December 2002.

[1] A new physical mechanism that is potentially relevant for the equilibrium morphodynamics of tide-dominated estuaries and in understanding the occurrence of lateral shoals in these systems is identified. The mechanism acts in relatively straight and wide channels (width of the order of the horizontal tidal excursion length) in which both external overtides and the Coriolis force affect sediment transport. This is investigated by analyzing an idealized model, which consists of the 3D shallow water equations, mass conservation for suspended load, and a bed evolution equation. The model is forced by a prescribed depth-averaged tidal current. It is demonstrated that, when viewed in the direction of the flood flow, a flood (ebb)-dominant current generates a net cross-sectional sediment transport to the left (right) in the Northern Hemisphere. A morphodynamic equilibrium is established by a counteracting dispersive sediment flux, generated by shear stresses that increase toward shallower water. This dispersive flux is much larger than the flux due gravitational downslope effects. The equilibrium bed profile has a constant slope in the lateral direction that varies as $\cos(\varphi)$, where φ is the phase difference between the M_2 and M_4 external horizontal tide. Hence, the smallest depths are found on the left (right) in case of a flood (ebb)-dominant current. Typical cross-channel depth differences may be as large as several meters. Velocity data collected in the Dutch Western Scheldt estuary are used to tune the hydrodynamic parameters in the model. Analysis of the bathymetric data seems to confirm the qualitative results of the model. *INDEX TERMS:* 4235 Oceanography: General: Estuarine processes; 4508 Oceanography: Physical: Coriolis effects; 4558 Oceanography: Physical: Sediment transport; 4560 Oceanography: Physical: Surface waves and tides (1255); *KEYWORDS:* equilibrium, morphodynamics, tidal channels, coriolis

Citation: Schramkowski, G. P., and H. E. de Swart, Morphodynamic equilibrium in straight tidal channels: Combined effects of Coriolis force and external overtides, *J. Geophys. Res.*, *107*(C12), 3227, doi:10.1029/2000JC000693, 2002.

1. Introduction

[2] Many tidal inlets and estuaries exhibit complex morphological patterns consisting of channels and shoals with strong spatial and temporal variability. As a prototype example one may consider the Western Scheldt (WS) estuary [*Van den Berg et al.*, 1990; *Jeuken*, 2000], which is situated at the outermost south-west part of Netherlands. On length scales of the order of the tidal excursion length (typically 10–20 km) the WS banks show meandering behavior. At relatively straight parts of the tidal channels and at their mutual intersections, so-called thresholds are found. These thresholds are regions of enhanced deposition which show fast shoaling when left to their own device. Both from a management and scientific point of view it is important to understand (and eventually predict) the behavior of these features.

[3] Traditionally, empirical and semiempirical models [cf. *De Vriend*, 1996, and references therein; *Van de Kreeke*, 1998] have been used to predict the response of tidal embayments to changes in external conditions. Such models are based on empirical relationships between various macroscale quantities characterizing the embayment. They are useful for long-term predictions, but they are not suitable to gain insight.

[4] The latter can be achieved by using quasi-realistic or complex process-oriented models, which describe the water motion, sediment transport and the evolution of the seabed according to basic physical principles. It has been shown [*Wang et al.*, 1995; *Verbeek et al.*, 1999] that complex numerical models, based on a quasi-3D description of the water motion and sediment transport, are able to simulate many characteristics of observed morphological phenomena in tidal embayments. These models are successful for simulation periods up to several decades; the authors of these papers attribute the inaccuracies on the longer term to the lack of process knowledge, in particular about 3D processes. Indeed there are indications, both from field data and model studies, that channels and thresholds arise from genuine three-dimensional processes. For instance, numerical simulations [*Verbeek et al.*, 1999] suggest that secondary circulations due

0148-0227/02/2000JC000693$09.00

to curvature are important for the existence of thresholds. This is in agreement with the outcome of field observations [*Jeuken*, 2000] which also indicate that 3D sediment lag affects appear to be important for threshold dynamics.

[5] Although complex 3D models will be the ultimate tool to be used for simulating the morphodynamics of tidal embayments, their success will highly depend on understanding and incorporating the essential physical mechanisms. For example, the formulation of the turbulent exchange of momentum and sediment in the water column and the bottom boundary conditions (for the shear stress and for the erosion and deposition fluxes) are crucial elements of such a model.

[6] These arguments motivate the study of idealized process-oriented models, in which highly schematized geometries and simplified versions of the full equations of motion are considered. Idealized models of tidal embayments have been mainly used in the context of depth-averaged formulations. With regard to the tidal motion *Speer and Aubrey* [1985], *Friedrichs and Madsen* [1992], *Friedrichs and Aubrey* [1994] and *Lanzoni and Seminara* [1998] have shown the importance of internally generated overtides, bottom friction, width convergence and the formulation for the frictional drag at the bottom. Idealized depth-averaged morphologic models for semienclosed tidal embayments were considered by *Schuttelaars and De Swart* [1996], *Schuttelaars and de Swart* [1999], *Schuttelaars and de Swart* [2000], *De Jong and Heemink* [1996] and *Van Leeuwen et al.* [2000]. They demonstrate that these models allow for primary morphodynamic equilibria which are characterized by a steady bottom profile with no structure in the cross-channel direction. For such systems it has been shown explicitly that channels and shoals develop as a result of the inherent instability of the primary equilibrium. For a short tidal embayment (length much smaller than the tidal wavelength) these morphodynamic equilibria describe a spatially uniform tidal motion over a bottom which slopes upward when moving from the entrance to the landward boundary, where a zero mass flux condition is applied. For longer embayments more concave bottom profiles are obtained. The properties of such equilibria, both with respect to tidal motion and bottom structure, appear to compare rather well with field observations [*Schuttelaars and de Swart*, 2000].

[7] A 3D idealized morphodynamic model of a tidal channel was studied by *Seminara and Tubino* [1998]. They considered the initial formation of bars in a channel with vertical nonerodible walls. They limited their investigation to a local analysis, i.e., they considered a stretch of the channel which scales with the channel width. This length scale was considered to be much smaller than any other longitudinal length scale, including the channel length, the tidal wavelength and the tidal excursion length (i.e., the horizontal distance traveled by a fluid particle during one tidal cycle with maximum velocity). As a result the effect of Coriolis forces could be neglected. Moreover, they assumed a frictionally dominant tidal channel (frictional decay timescale much smaller than the tidal period) and included only a single external M_2 tidal constituent. They observed that their primary morphodynamic equilibrium constitutes a horizontal bottom.

[8] However, the model of *Seminara and Tubino* [1998] is not directly applicable to embayments such as the WS. One reason is that this embayment is not frictionally dominant (in fact local inertial terms in the momentum equations have a similar magnitude as frictional terms). Furthermore, its width is not small compared to the tidal excursion length; this implies that effects of Earth rotation cannot be a priori neglected, because the Coriolis force (driving the circulation superimposed on the primary depth-averaged current) has the same order of magnitude as the inertial contributions. Finally, in the WS significant overtides are present which enter the domain through the seaward boundary.

[9] In the present paper we will extend the model of *Seminara and Tubino* [1998] by including the effects of Coriolis forces, external overtides and local inertial terms. The main objective is to describe a new physical mechanism which is potentially important to understand the formation of lateral shoals in strongly tidal estuaries. Such lateral shoals not only occur in the WS, but also in, e.g., James River [*Valle-Levinson et al.*, 2000]. The mechanism involves the joint action of Coriolis force and external overtides in driving transverse circulations of water and of sediment. It will be shown that, under these circumstances, lateral shoals must be present to maintain morphodynamic equilibrium. This will be demonstrated explicitly with a model in which it is assumed that the current and bottom are uniform in the along-channel direction. Knowing the properties of this morphodynamic equilibrium is also crucial to model and understand the formation of more complex bottom patterns which have both a lateral and longitudinal structure. Hence the present study serves as a first step toward this understanding.

[10] The paper is organized as follows. In section 2 the model is described and in section 3 the modeled tidal current profiles are compared with field data of the WS. In section 4, it is shown that a morphodynamic equilibrium under the combined effect of Coriolis force and external overtides cannot constitute a horizontal bottom. Also, a method to obtain such nonhorizontal equilibrium profiles is outlined and its results are presented in section 5. To gain support for these results, they are compared with bathymetric data from the WS estuary. Here the emphasis is, of course, on global phenomena, as the present model is not designed to yield a detailed description of the morphology of the WS. Section 6 discusses the model results and outlines possible future work while section 7 briefly mentions the main conclusions.

2. Model Formulation

2.1. Model Setup

[11] We consider an infinitely long channel of constant width B with straight, nonerodible side banks at $y = 0, B$. The water motion is driven by external M_2 and M_4 tides, with $\sigma = 1.4 \times 10^{-4}\mathrm{s}^{-1}$ denoting the angular frequency of the M_2 tide. The characteristic tidal velocity amplitude in the channel is $U \sim 1\ \mathrm{ms}^{-1}$. It is assumed that B is of the same order of magnitude as the horizontal tidal excursion length $l_m = U/\sigma$. The bottom is situated at $z = z_b$, measured with respect to a horizontal reference plane at $z = 0$, while the free water surface is given by $z = \zeta(x, y, t)$ (see Figure 1). The longitudinal (i.e., along-channel) direction is denoted by x. The model is local in that it does not describe an entire tidal embayment: rather, we consider a longitudinal portion of a few tidal excursion lengths.

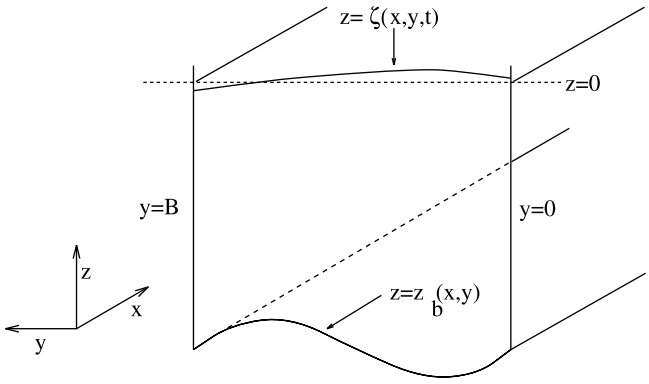

Figure 1. Sketch of the channel geometry in order to illustrate the definitions of water level and bottom depth.

[12] As we are interested in genuine 3D morphodynamics, the fluid flow is described by the so-called 3D shallow water equations which allow for vertical velocities but still assume hydrostatic equilibrium. Since we consider WS-type estuaries where the sediment consists of fine sand and tidal velocities reach values up to 1 m s^{-1}, the sediment is mainly transported as suspended load. Finally, net (i.e., tidally mean) divergences and convergences of sediment fluxes determine the bottom evolution. Here we are interested in large-scale bottom structures (length scales of the order of the tidal excursion length). The so-called morphodynamic timescale, on which these bottom patterns evolve, is much longer (order of decades) than the tidal period. The channel geometry explicitly enters the model through impermeability of the sidewalls while bottom and surface boundary conditions are included by a partial slip assumption and a stress-free surface condition, respectively.

[13] Finally, the model adopts a rigid lid approximation, which implies that water level ζ and its spatial gradients may be neglected everywhere except for the terms that describe the forcing by the external tide. This implies that the characteristic scale of sea surface elevations is considered to be small with respect to the typical water depth.

2.2. Model Equations

[14] We will now briefly discuss the model equations. We consider equilibrium morphodynamics in a system with along-channel symmetry, i.e., local longitudinal variations will be omitted except for water level gradients which describe forcing by the externally imposed tide as well as effects induced by the Coriolis force.

2.2.1. Tidal Hydrodynamics

[15] The hydrodynamics of the model is governed by the so-called three-dimensional shallow water equations [*Vreugdenhil*, 1994]:

$$\frac{\partial u}{\partial t}+v\frac{\partial u}{\partial y}+w\frac{\partial u}{\partial z}-fv=-g\frac{\partial \zeta}{\partial x}+\frac{\partial}{\partial z}\left(A_v\frac{\partial u}{\partial z}\right), \tag{1}$$

$$\frac{\partial v}{\partial t}+v\frac{\partial v}{\partial y}+w\frac{\partial v}{\partial z}+fu = g\frac{\partial \zeta}{\partial y}+\frac{\partial}{\partial z}\left(A_v\frac{\partial u}{\partial z}\right), \tag{2}$$

$$\frac{\partial v}{\partial y}+\frac{\partial w}{\partial z}=0, \tag{3}$$

where u, v and w denote the along-channel, lateral and vertical velocity components, respectively, while ζ is the water level with respect to the reference plane (see Figure 1). The quantities f and g are the Coriolis parameter and the gravitational acceleration. It will be assumed henceforth that the vertical turbulent viscosity coefficient A_v is time-independent. Measurements have shown that time-independent turbulent viscosity coefficients in general can reproduce velocity profiles and bottom shear stresses quite satisfactorily [e.g., *Wiberg*, 1995], at least for circumstances when the flow is not strongly turbulent [*Davies and Villaret*, 1999]. For the time being, it is also assumed that A_v does not vary throughout the water column. The discussion about the dependence of A_v on the water depth will be postponed until section 5. At the water surface $z = 0$ we assume the water motion to be stress free and to obey the kinematic boundary condition:

$$A_v\frac{\partial u}{\partial z}=A_v\frac{\partial v}{\partial z}=0, \quad w=0 \quad \text{at} \quad z=0, \tag{4}$$

the latter statement being a result of the rigid lid approximation.

[16] The boundary conditions at the bottom ($z = z_b$) are given by the so-called partial slip condition while the vertical velocity is found from impermeability:

$$A_v\frac{\partial u}{\partial z}=su, \quad A_v\frac{\partial v}{\partial z}=sv, \quad w=v\frac{\partial z_b}{\partial y} \quad \text{at} \quad z=z_b. \tag{5}$$

The parameter s is the so-called stress parameter. It can be used to tune the bottom boundary condition to mimic any situation ranging from a stress free bottom ($s = 0$) to a no-slip bottom ($s \to \infty$). Both A_v and s will hereafter be referred to as friction parameters. The partial slip model was already applied to tidal flows by *Prandle* [1982] and *Maas and van Haren* [1987], but its use goes back a long way [see *Rozovskii*, 1961, and references therein]. Physically, it is a relation between shear stress and velocity at the top of the bottom boundary layer rather than at the true boundary $z = z_b$. However, as the stress throughout the lower layer is approximately constant, equation (5) yields the stress that acts on the bed and governs erosion of sediment.

[17] In the lateral direction, sidewall impermeability has to be incorporated. Strictly speaking, this implies $v(0) = v(B) = 0$ at $y = 0$, B which in turn requires detailed knowledge of (thin) viscous boundary layers near the bank and the incorporation of horizontal dispersion terms in the momentum equations (1)–(2). As an alternative, we exclude these horizontal dispersion terms and thereby do not interpret $y = 0$, B as the position of the sidewalls, but as the positions where the interface between bulk flow and sidewall boundary layers is situated. In that case, impermeability indicates that the lateral water flux should be zero at any moment, i.e.,

$$\bar{v}=0 \quad \text{at} \quad y=0,\ B, \tag{6}$$

where the vertical average is defined for any quantity $Q(x, y, z, t)$ as

$$\bar{Q}\equiv\frac{1}{-z_b}\int_{z_b}^{0}Q\,dz. \tag{7}$$

Now, from equations (3)–(5) it follows that $\partial\bar{v}/\partial y = 0$, hence impermeability (6) implies

$$\bar{v} = 0 \quad \text{everywhere.} \tag{8}$$

[18] Finally, we remark that the external tidal forcing in equations (1) and (2) needs to be specified in order to have a closed formulation for the hydrodynamics. This is done by prescribing the vertical average of the externally generated tidal flow:

$$\bar{u} = U[\cos(\sigma t) + \beta\cos(2\sigma t - \varphi)], \quad \bar{v} = 0, \tag{9}$$

Here, as stated before, U and $\sigma = 1.4 \times 10^{-4}$ s^{-1} denote the velocity amplitude and angular frequency of the external M_2 tide, respectively. The properties of the external M_4 tide are completely specified by its relative strength β and the phase difference φ with respect to the external M_2 tide. For typical WS situations, $U \approx 1$ m s^{-1}} and $\beta \approx 0.1$ while varies φ gradually along the estuary [*Van den Berg et al.*, 1990; *Jeuken*, 2000].

2.2.2. Sediment Dynamics

[19] Next, let us elaborate on the transport of sediment in suspension. This is described by the concentration equation

$$\frac{\partial c}{\partial t} + \frac{\partial (vc)}{\partial y} + \frac{\partial[(w - w_s)c]}{\partial z} = \frac{\partial}{\partial y}\left(K_h \frac{\partial \langle c\rangle}{\partial y}\right) + \frac{\partial}{\partial z}\left(K_v \frac{\partial c}{\partial z}\right), \tag{10}$$

where the settling velocity w_s and the lateral dispersion coefficient K_h will be assumed constant hereafter; typical values for these model parameters are $w_s = 0.02$ m s^{-1} (fine sand, grain size $\approx$200 μm) and $K_h = 20$ m^2 s^{-1}, respectively. Furthermore we will assume that vertical dispersion coefficient K_v has the same vertical structure as A_v, i.e., $K_v = A_v$; this agrees qualitatively with results from literature [e.g., *Van Rijn*, 1984] which state that $K_v = \nu A_v$ where ν is of order unity. The brackets ($\langle\rangle$) denote tidal average which is defined for any quantity $Q(x, y, z, t)$ as

$$\langle Q\rangle \equiv \frac{1}{P}\int_0^P Q\,\mathrm{d}t, \tag{11}$$

where $P = 2\pi/\sigma$ denotes the period of the M_2 tide.

[20] Note that in equation (10) horizontal dispersion of only the residual concentration is taken into account. This is a necessary mechanism, as will be now explained. It has been mentioned before that large-scale bottom evolution occurs on timescales that are much longer than the tidal period. Hence this evolution is governed by tidally averaged sediment fluxes and divergences thereof rather than by their instantaneous values. Along the lines of reasoning that have been outlined above for fluid flow, it is then found that sidewall impermeability to sediment implies that the tidal mean of the lateral sediment mass transport per unit width $\mathcal{F}$ should vanish at $y = 0, B$, i.e.,

$$\mathcal{F} \equiv z_b\left\{\langle\overline{vc}\rangle - K_h\frac{\partial\langle\bar{c}\rangle}{\partial y}\right\} = 0 \text{ at } y = 0,\ B. \tag{12}$$

In general, the advective part $\langle\overline{vc}\rangle$ of $\mathcal{F}$ is nonzero, despite the fact that $\bar{v} = 0$ (see equation (8)). Thus equation (12) indicates that impermeability can only be established by including lateral dispersion of residual concentration while no such effect is required regarding the time varying part of c. This is our main motivation to include the first term on the r.h.s. of equation (10).

[21] Let us now turn to the vertical boundary conditions for equation (10). At the water surface $z = 0$ no sediment particles are leaving or entering through the boundary, which is expressed by the statement

$$w_s c + K_v\frac{\partial c}{\partial z} = 0 \text{ at } z = 0. \tag{13}$$

At the bottom, the normal component of the sediment flux entering the fluid is given by the difference between erosion and deposition, $S_\star$:

$$-n_y K_h\frac{\partial\langle c\rangle}{\partial y} - n_z\left(w_s c + K_v\frac{\partial c}{\partial z}\right) = S_\star, \tag{14}$$

at $z = z_b$. Here $\hat{\mathbf{n}} = (0, n_y, n_z)$ is the upward directed unit normal vector at the bottom.The erosion-deposition flux

$$S_\star = w_s(c_a - c_b), \tag{15}$$

is related to the sediment concentration c_b at the bottom and the so-called reference concentration c_a. The latter is a function of the magnitude of the bed shear stress $\tau = \rho A_v\|\partial(u, v)/\partial z\|_{z=z_b}$, where ρ is the density of the water, and is parameterized as [*Dyer*, 1986, p. 168]

$$c_a = \gamma\rho_s(1 - p)\frac{\tau}{\tau_c}. \tag{16}$$

Here $\gamma \approx 7.8 \times 10^{-5}$, while ρ_s, p and τ_c denote the density and porosity of the sediment and the critical shear stress for erosion, respectively. For the sediment under consideration (fine sand), typical values for the latter three parameters are $\rho_s = 2650$ kg m^{-3}, $p = 0.4$ and $\tau_c = 0.1$ N m^{-2}, respectively. In obtaining (16) from *Dyer*'s [1986] expression, it has been assumed that $\tau \gg \tau_c$ throughout the tidal cycle.

2.2.3. Bottom Evolution

[22] Finally, the time evolution of the bed $z_b(x, y, t)$ is found from

$$\frac{\partial z_b}{\partial t} = -\frac{\langle S_\star\rangle}{\rho_s(1 - p)}, \tag{17}$$

where the r.h.s. of equation (17) describes the bottom change due to net deposition of suspended sediment. This term can also be written in flux form by deriving an expression for $\langle S_\star\rangle$ from integrating the concentration equation (10) over the depth and applying boundary conditions (13) and (14). In using equation (17) it is assumed that the tidal period is small compared to the timescale of bottom evolution, as is the case for the features studied in this paper, see also section 2.1. As a result, bottom evolution is not sensitive to the instantaneous rate of erosion and deposition but rather to their tidal means: this is expressed by the tidally averaged erosion-deposition function on the r.h.s. of equation (17). As we

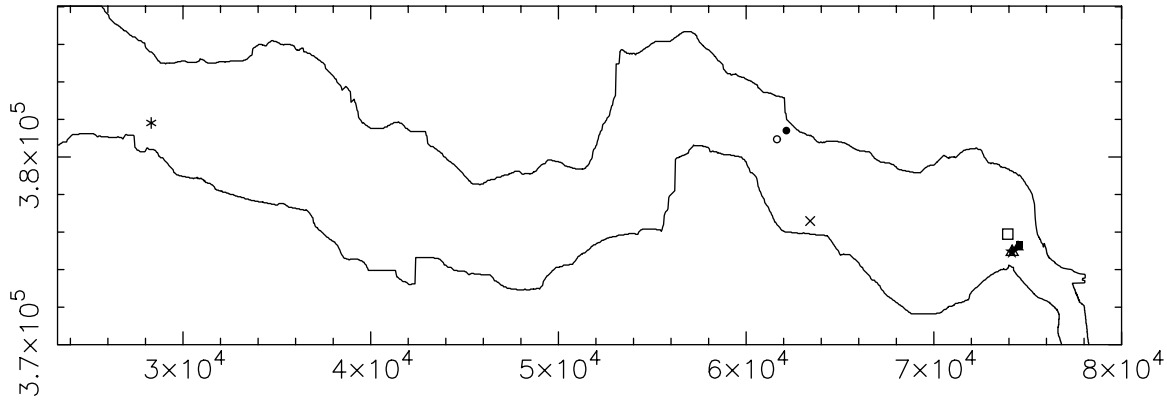

Figure 2. Location of the field sites inside the WS from which the data discussed in this paper are taken. For relation between markers and data sets, see Table 1. The units on the axes are meters.

consider equilibrium morphodynamics in this paper, we take $\langle S_\star \rangle = 0$.

3. Friction Parameters From Field Data

3.1. Data Processing and Fitting Procedure

[23] We have used data of velocity measurements carried out in the WS estuary in order to obtain realistic estimates for the parameters A_v and s. To this end, a number of 9 data sets from different field campaigns during the period 1970–1981 were processed. The specific emphasis was on the vertical structure of the M_2 tidal velocity field, being the dominant component of the water motion. The sets all comprised a full M_2 tidal period so that it was possible in principle to perform harmonic analysis. Typically, the sets contained data that were taken at least at an hourly frequency while information about the vertical structure was inferred from five points inside the water column. The error in the velocity date was not specified and was estimated at 5 cm s^{-1}. The lowest registration point was located at approximately 1 m above the bottom: this is usually believed to be the level where the top of the bottom boundary layer resides, i.e., where the partial slip condition may be applied.

[24] Figure 2 shows the location of the field sites within the WS estuary. Half of the data sets (M152-M165, see also Table 1) were taken around the so-called region of Bath, the rest was more spread over the estuary.

[25] The data described above were processed as follows. First, the direction of the main tide was determined as the direction in which the tidally averaged kinetic energy was maximum. Second, all instantaneous velocity measurements were projected along this direction. Next, these measurements were interpolated on an equidistant, time-independent vertical grid of points. Finally, the M_2-component $\hat{\mathcal{U}}(z, t)$ of the resulting signal was obtained by harmonic analysis with the result

$$\hat{\mathcal{U}}(z,t) = \hat{\mathcal{U}}_c(z)\cos(\sigma t) + \hat{\mathcal{U}}_s(z)\sin(\sigma t).$$

The model parameters A_v and s were obtained by a least squares fitting of the theoretical profile $u(z, t)$, that is a solution to equations (1)–(5) for flow over a horizontal bottom, to $\hat{\mathcal{U}}(z, t)$. This theoretical profile (including the effects of the Coriolis force) is discussed by *Prandle* [1982] and *Maas and van Haren* [1987].

[26] The motivation for choosing this procedure is that, as stated before, the M_2 tidal constituent dominates the water motion in the WS. Furthermore, it is assumed that this M_2 tide is mainly due to the interaction of the tidal wave with the large-scale geometry of the WS. In other words, generation of M_2 tidal currents due to local topography and nonlinear interactions between different tidal constituents are assumed to be an order of magnitude smaller. As long as local topographic variations are small

Table 1. Vertical Viscosity A_v and Friction Parameter s as Derived From the Data Set Described in the Main Text[a]

Data Set	Symbol	H, m	A_{v0}, $m^2\ s^{-1}$	$A_v/(\sigma H^2)$	s_0, m s^{-1}	$s_0/(\sigma H)$
M32	*	12.90	0.207 ± 0.038	8.89 ± 1.64	0.017 ± 0.0011	9.57 ± 0.62
M104	×	13.32	0.062 ± 0.007	2.48 ± 0.29	$0.007 \pm 8 \times 10^{-4}$	5.76 ± 0.45
M105	○	10.19	0.069 ± 0.016	4.73 ± 1.11	$0.007 \pm 6 \times 10^{-4}$	4.92 ± 0.41
M115	●	8.61	0.093 ± 0.020	8.99 ± 1.90	$0.011 \pm 7 \times 10^{-4}$	8.73 ± 0.60
M152	□	9.23	0.110 ± 0.022	9.19 ± 1.86	$0.008 \pm 4 \times 10^{-4}$	6.04 ± 0.28
M160	△	18.86	0.185 ± 0.032	3.71 ± 0.64	$0.012 \pm 9 \times 10^{-4}$	4.71 ± 0.33
M161	▲	11.53	0.096 ± 0.021	5.18 ± 1.10	$0.007 \pm 4 \times 10^{-4}$	4.24 ± 0.26
M162	■	7.48	0.077 ± 0.023	9.83 ± 2.93	$0.007 \pm 5 \times 10^{-4}$	6.73 ± 0.52
M165	★	19.24	0.375 ± 0.066	7.24 ± 1.28	0.024 ± 0.0016	8.97 ± 0.63

[a]Here, "symbol" refers to the markers used in Figure 2, while H denotes the tidally averaged water depth.

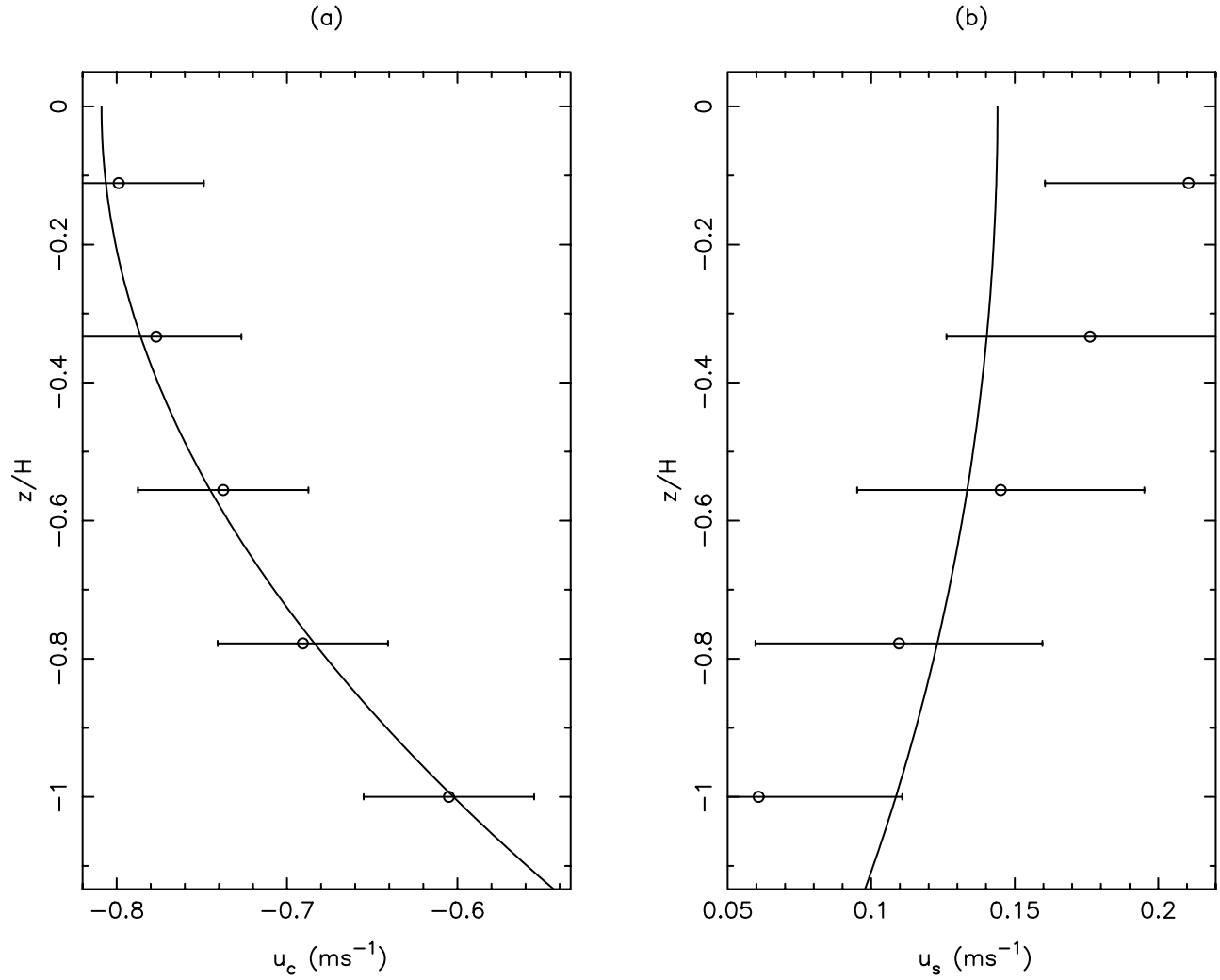

Figure 3. Comparison between measurements (open circles) and best fit for partial slip (solid line) for (a) cosine and (b) sine component of the fit (data set M162). The error bars reflect a presumed error of 5 cm s^{-1} in the data while H denotes the tidally averaged water depth. The lowest data point is at 1 m above the true bottom.

compared to the mean water depth (as is the case for all sites shown here) this is a good approximation.

3.2. Values of Partial Slip Parameters

[27] Figure 3 shows a typical result for vertical velocity profiles that were obtained from fitting the partial slip model to the data. It appears that the simple partial slip model is suitable to model the gross characteristics of the observed tidal velocity field, and thereby of the bed shear stress and the resulting sediment pick-up function. Of course, for a more detailed description a much more sophisticated turbulence closure scheme is needed.

[28] Table 1 shows the results for the partial slip parameters A_v and s. We see that the dimensional values for A_v show significant variation, even when taken in more or less the same region of the WS (as is the case for M152-M165). Typically, we find turbulent viscosity coefficients that have dimensional values between 0.06 and 0.35 $m^2\ s^{-1}$. This strong variation may be attributed to the complex local bathymetry, the neglect of advective acceleration terms in the adopted theoretical profile and the short time record of the data sets. The dimensional value of the stress parameter s shows milder variation: it varies from 0.007 to 0.024 m s^{-1}. When expressed nondimensionally as $A_v/(\sigma H^2)$ and $s/(\sigma H)$, where H is the local water depth, the friction parameters have values between 2.5 and 10, with a preference for higher values (above 5). Dimensionless values for A_v and s quoted elsewhere in the literature [*Prandle*, 1982; *Maas and van Haren*, 1987] refer to North Sea data and indicate that $1 \leq A_v/(\sigma H^2) \leq 5$ and $0.1 \leq s/(\sigma H) \leq 10$. Hence the results displayed in Table 1 seem to imply that vertical viscosity plays a larger role in the WS as compared to the North Sea, while its stress parameter values are at the high end of the presumed range $0.1 \leq s \leq 10$.

[29] The bathymetric contribution to the variation in the friction parameters may be modeled by allowing A_v and s to depend upon the local water depth H. This can be justified by a mixing length argument, which leads to a power law scaling [*Friedrichs and Hamrick*, 1996], i.e.,

$$A_v = A_{v0}\left(\frac{H}{H_0}\right)^n \quad , \quad s = s_0\left(\frac{H}{H_0}\right)^m .$$

Table 2. Characteristics of the Vertically Averaged External Tide as Derived From Field Data

Data Set	U, m s^{-1}	β	φ
M32	0.99 ± 0.05	0.19 ± 0.05	−1.70
M104	1.07 ± 0.05	0.24 ± 0.05	−3.15
M105	0.77 ± 0.05	0.31 ± 0.07	−1.59
M115	0.91 ± 0.05	0.31 ± 0.06	−1.62
M152	1.30 ± 0.05	0.10 ± 0.04	−2.23
M160	0.97 ± 0.05	0.21 ± 0.05	0.63
M161	1.02 ± 0.05	0.08 ± 0.05	−0.69
M162	0.75 ± 0.05	0.09 ± 0.07	−0.60
M165	0.93 ± 0.05	0.17 ± 0.05	0.17

When applying this to the present data set, a power law fit yields

$$A_{v0} = (0.096 \pm 0.019)\ \mathrm{m^2 s^{-1}},$$
$$s_0 = (0.0087 \pm 0.0015\ )\mathrm{ms^{-1}},$$
$$n = 1.28 \pm 0.48\ ,\ m = 0.88 \pm 0.40,$$

where H_0 = 10 m was chosen. We remark that the value for n is in agreement with the range n = 1–1.5 which *Friedrichs and Hamrick* [1996] report for well-mixed estuaries. Finally, Table 2 shows the properties of the external M_2 and M_4 tides (cf. equation (9)) that follow from the data set. We see that the typical M_2 tidal amplitude is of the order of 1 m s^{-1} while an average value of the overtide strength β is approximately 0.2.

[30] Note that the values of the phase difference φ show a rather strong spatial variation, as can be seen from the sets M152-M165 that are located close together. This is probably due to the excitation of internal overtides by tide-topography interaction. As the present model requires input related to external tides, we have taken φ values from a one-dimensional (depth and width averaged) WS-model by *Schuttelaars and de Swart* [2000]. The values of U and β listed in Table 2 show good agreement with the results from this model.

3.3. Scaled and Default Parameter Values

[31] Table 3 shows parameter values that are representative for typical WS circumstances. These values are taken to be default in the remainder of this paper and will always be assumed to apply, unless stated otherwise. Note that some parameters are also expressed in nondimensional units for future reference. Finally, we restate the power law dependence of A_v and s on water depth $-z_b$

$$A_v = A_{v0}\left(\frac{z_b}{z_{b0}}\right)^n\ ,\quad s = s_0\left(\frac{z_b}{z_{b0}}\right)^m, \tag{18}$$

where hereafter the parameters are taken from Table 3 with $z_{b0} = -H = -10$ m.

4. Equilibrium Bottom Profiles

[32] Due to the Coriolis force, the hydrodynamics in longitudinal and lateral direction are coupled. As explained in the introduction, it is to be expected that Coriolis effects will also affect morphodynamics. For instance, when considering equilibrium bottom profiles one may expect non-horizontal bottom configurations to occur. Here we will show that our simple channel model does allow for a horizontal equilibrium bottom provided that there is only one tidal component in the flow or no Coriolis effects. For the more realistic case of external overtides and influence of Earth rotation, a laterally sloping bottom appears inevitable. Of course, this has profound implications for, say, the stability properties of bottom patterns.

[33] As can be seen from equations (14) and (17) a morphodynamic equilibrium is defined by a balance between net erosion and deposition fluxes at the bed level. From averaging of the concentration equation (10) over depth and tidal period it then follows that the net lateral sediment mass flux per unit width $\mathcal{F}$, defined in equation (12), should satisfy

$$\mathcal{F} = z_b\left\{\langle\overline{vc}\rangle - K_h\frac{\partial\langle\overline{c}\rangle}{\partial y}\right\} = 0 \text{ everywhere.} \tag{19}$$

This condition will be used hereafter as a criterion for morphodynamic equilibrium.

4.1. Horizontal Bottom Profiles

[34] For the case of a horizontal bottom ($z_b = -H$ = constant, i.e., no cross-channel structure) with a single external tidal forcing, the 3D shallow water equations allow for a fluid motion with zero vertical velocity and horizontal velocities that depend only on time and depth as follows:

$$u(z,t) = u_c(z)\ \cos(q\sigma t) + u_s(z)\ \sin(q\sigma t), \tag{20}$$

$$v(z,t) = v_c(z)\ \cos(q\sigma t) + v_s(z)\ \sin(q\sigma t), \tag{21}$$

where q is an integer such that $q\sigma$ is the frequency of the external tide. In that case nonlinear advective terms are absent from (1) and (2); for explicit forms of (20) and (21), see, e.g., *Maas and van Haren* [1987]. When several external tidal modes are present, the resulting velocity field is obtained by linear superposition of modes with the structure as given in (20) and (21). The cross-channel flow (21) arises from the interaction of the along-channel motion with the Coriolis force and has the same frequency as the imposed external tide [*Prandle*, 1982].

[35] It will be shown that the above 3D flow also corresponds to a morphodynamic equilibrium provided that only a single external tide is present. First we note that the flow, and thereby the corresponding concentration, has no

Table 3. Dimensional and Dimensionless Values for Default Parameter Values Adopted in This Paper[a]

Quantity	Dimensional Value	Nondimensional Scaling	Scaled Value
H	10 m	–	1.0
U	1 m s^{-1}	–	1.0
β	–	–	0.2
A_{v0}	0.084 m^2 s^{-1}	$A_{v0}/(\sigma H^2)$	6.0
s_0	0.0084 m s^{-1}	$s_0/(\sigma H)$	6.0
K_{v0}	0.084 m^2 s^{-1}	$K_{v0}/(\sigma H^2)$	6.0
K_h	20.0 m^2 s^{-1}	$\sigma K_h/U^2$	0.0028
w_s	0.02 m s^{-1}	$w_s/(\sigma H)$	14.3
m	–	–	1
n	–	–	1

[a]For further explanation, see main text.

structure in the cross-channel direction. Consequently, the contribution of dispersive flux in equation (19) vanishes. Next, we use the fact that the concentration equation (equation (10)) is forced by the *magnitude* of the bottom shear stress rather than its direction. As a result, the sediment concentration can be written as a Fourier series which contains only a residual term, a contribution at frequency $2q\sigma$ and its overtides (with frequencies $4q\sigma$, $6q\sigma$, etc.). There is, however, *no* contribution at frequency $q\sigma$ itself. From (21) we then find that $\langle\overline{vc}\rangle$ vanishes identically which implies $\mathcal{F} = 0$, hence from (19) it follows that this is a morphodynamic equilibrium.

4.2. Overtides and Nonhorizontal Bottom Profiles

[36] From the analysis presented in section 4.1 it follows that $\langle\overline{vc}\rangle$ will generally not vanish if an external overtide is simultaneously present along with Coriolis effects. In that case, both v and c have contributions that oscillate at frequency $2q\sigma$ (i.e., that of the external overtide), yielding a nonvanishing $\langle\overline{vc}\rangle$. Consequently, an equilibrium bottom must show lateral variation in order to generate a dispersive sediment flux, or a sediment flux induced by gravitational (downslope) effects, to compensate for the net advection of sediment (second term on r.h.s. of equation (19)).

[37] For completeness, we point out that a horizontal equilibrium bed is always recovered (even in the presence of external overtides) when Coriolis effects are absent since the lateral circulations that drive the nonzero lateral sediment flux will then not occur. We want to emphasize that the tilting bottom is a robust phenomenon. In general, it only requires the presence of both Coriolis force and an even external overtide of the main tidal forcing. Parameterizations of bottom shear stress are only required to depend upon the *magnitude* of velocity, but this is seldom a severe restriction.

4.3. Computation of the Lateral Bottom Variation

[38] In the remainder of this section, we will outline how the lateral variation of the equilibrium bottom can be obtained when the channel system is forced with an M_2 tide and an M_4 overtide as specified in equation (9).

[39] We consider a tidal channel of width on the order of the tidal excursion length $l_m = U/\sigma$, which is small compared to the Rossby radius of deformation $R = \sqrt{(gH)}/f$. We therefore expect that the lateral bottom profile of the channel can be written as a Taylor expansion around $y = B/2$ which can be approximated by the linear relation:

$$z_b = -H + \beta h(y) \quad , \quad \frac{h(y)}{H} = \lambda\left(\frac{y}{B} - \frac{1}{2}\right), \tag{22}$$

the error of truncation being $O((l_m/R)^2)$. Thus the problem of solving the bottom profile is reduced to finding the lateral tilt λ.

[40] Apart from (22) it is also assumed that the imposed M_4 overtide is weak (i.e., $\beta \ll 1$). As a result, all quantities can be expanded as

$$Q = Q_0 + \beta Q_1 + \beta Q'(y,z,t), \tag{23}$$

where subscripts 0 and 1 denote the known solutions for a single M_2 and M_4 tide over a horizontal bottom (cf. equations (20) and (21)), respectively, while primes refer to the correction terms due to the sloping bottom. Since the generation of the primed quantities involves interaction with the zeroth order flow (see below), we will assume them to contain M_0, M_2 and M_4 modes while higher order harmonics will be neglected.

[41] Finally, we note that the friction parameters A_v and s will be taken to have a power law dependence on the water depth $-z_b$ as indicated by the results of section 3.2 (see equation (18)). For bed profile (22) this implies that these quantities can be expressed as

$$A_v = A_{v0} + \beta A'_v(y) \quad , \quad s = s_0 + \beta s'(y), \tag{24}$$

where subscripts 0 refer to values for water depth H while $A'_v(y) = -nA_{v0}h(y)/H$ and $s'(y) = -ms_0h(y)/H$.

[42] Below, we will first solve the flow induced by the tilt in the bottom (hereafter referred to as the induced flow). Next, the corresponding induced sediment distribution is obtained. Finally, these two features are combined into an expression for the equilibrium bottom tilt λ.

4.3.1. Solution of the Water Motion

[43] Inserting expansions (23), (22) and (24) into equations (1)–(3) and linearization yields the following equations for u', v' and w':

$$\frac{\partial u'}{\partial t} + v_0\frac{\partial u'}{\partial y} + w'\frac{\partial u_0}{\partial z} - fv' = -g\frac{\partial \zeta'}{\partial x} + A_{v0}\frac{\partial^2 u'}{\partial z^2} + A'_v(y)\frac{\partial^2 u_0}{\partial z^2}, \tag{25}$$

$$\frac{\partial v'}{\partial t} + v_0\frac{\partial v'}{\partial y} + w'\frac{\partial v_0}{\partial z} + fu' = -g\frac{\partial \zeta'}{\partial y} + A_{v0}\frac{\partial^2 v'}{\partial z^2} + A'_v(y)\frac{\partial^2 v_0}{\partial z^2}, \tag{26}$$

$$\frac{\partial v'}{\partial y} + \frac{\partial w'}{\partial z} = 0, \tag{27}$$

with surface boundary conditions

$$A_{v0}\frac{\partial u'}{\partial z} = A_{v0}\frac{\partial v'}{\partial z} = w' = 0. \tag{28}$$

At the bottom, a Taylor expansion around $z_b = -H$ now gives

$$A_{v0}\frac{\partial \mathbf{u}'}{\partial z} + A'_v(y)\frac{\partial \mathbf{u}_0}{\partial z} = s_0\mathbf{u}' + h(y)\left[s_0\frac{\partial \mathbf{u}_0}{\partial z} - A_{v0}\frac{\partial^2 \mathbf{u}_0}{\partial z^2}\right] + s'(y)\mathbf{u}_0, \tag{29}$$

$$w' = v_0(-H,t)\frac{\mathrm{d}h}{\mathrm{d}y}, \tag{30}$$

where $\mathbf{u}' = (u', v')$ and similarly for $\mathbf{u}_0$. The terms between square brackets account for the change in both the shear stress and the velocity when moving from the horizontal level ($z = -H$) to the actual bottom level at $z = -H + \beta h$.

[44] The impermeability condition (equation (8)) implies for the induced lateral velocity:

$$\overline{v'} = v_0(-H,t)\frac{h(y)}{H}, \tag{31}$$

where linearization implies that henceforth $^-$ should be interpreted as (7) with $z_b = -H$.

[45] The induced flow is forced by the interaction between the external M_2 tide and the tilting bottom: this is expressed by the bottom boundary conditions (29) and (30). Next, the M_0 and M_4 components are excited through the advection terms in the momentum equations (25) and (26) by interaction between the induced M_2 flow and the external M_2 tide. Hence, the M_0 and M_4 components are generated indirectly by the bottom tilt: as a consequence, we expect them to be weaker than the M_2 part of the induced flow.

[46] From equations (25)–(27) and the boundary conditions at the bottom it follows that u', v' and the induced water level gradient should have the following spatial structure:

$$u' = \frac{\mathrm{d}h}{\mathrm{d}y} F_u(z,t) + \frac{h(y)}{H} G_u(z,t), \tag{32}$$

and similarly for v' and $\nabla\zeta'$. The function $F_u(z, t)$ consists of a time-independent (M_0) part and a contribution at twice the basic frequency (M_4 component), while $G_u(z, t)$ describes the M_2 component of the solution. The induced vertical velocity w' only contains an M_2 component while its lateral structure scales with $\mathrm{d}h/\mathrm{d}y$ rather than $h(y)/H$. Due to the linearity of $h(y)$, M_6 and higher order tidal constituents cannot be excited through advection so that the induced flow only contains M_0, M_2 and M_4 components.

[47] Solution (32) indicates that the lateral structure can be separated out, meaning that for a single tidal component the y-dependence drops out of equations (25)–(30). The results are ordinary differential equations for the vertical structure of the Fourier coefficients of the solutions. The latter are solved by standard numerical (spectral) methods.

4.3.2. Solution of the Sediment Concentration

[48] In a similar way as for the fluid quantities, the time evolution of the induced sediment field is found to be governed by

$$\frac{\partial c'}{\partial t} + v_0 \frac{\partial c'}{\partial y} + w' \frac{\partial c_0}{\partial z} - w_s \frac{\partial c'}{\partial z} = K_\mathrm{h} \frac{\partial^2 \langle c' \rangle}{\partial y^2} + K_{\mathrm{v}0} \frac{\partial^2 c'}{\partial z^2} + K'_\mathrm{v}(y) \frac{\partial^2 c^0}{\partial z^2}, \tag{33}$$

where the term containing $K'_\mathrm{v}(y) = -nK_{\mathrm{v}0}h(y)/H$ stems from the assumption $K_\mathrm{v} = A_\mathrm{v}$. The boundary conditions at the surface and bottom are given by:

$$K_{\mathrm{v}0} \frac{\partial c'}{\partial z} + w_\mathrm{s} c' = -K'_\mathrm{v}(y) \frac{\partial c_0}{\partial z}, \tag{34}$$

$$K_{\mathrm{v}0} \frac{\partial c'}{\partial z} + K'_\mathrm{v}(y) \frac{\partial c_0}{\partial z} = -w_\mathrm{s} \Gamma \tau' - h(y) \left[w_\mathrm{s} \Gamma \frac{\partial \tau_0}{\partial z} + K_{\mathrm{v}0} \frac{\partial^2 c_0}{\partial z^2} \right], \tag{35}$$

respectively, where $\Gamma = \gamma\rho_\mathrm{s}\ (1 - p)/\tau_\mathrm{c}$. Furthermore the quantities τ_0 and τ' are contributions to the magnitude of the full stress τ. Defining $\mathbf{u} = (u, v)$ as the total horizontal velocity vector, the latter to $O(\beta)$ can be written as:

$$\tau \equiv \rho A_\mathrm{v} \left| \left| \frac{\partial \mathbf{u}}{\partial z} \right| \right| = \rho A_{\mathrm{v}0} \left[\left(\frac{\partial \mathbf{u}_0}{\partial z} + \beta \frac{\partial \mathbf{u}_1}{\partial z} + \beta \frac{\partial \mathbf{u}'}{\partial z} + \beta \frac{A'_\mathrm{v}(y)}{A_{\mathrm{v}0}} \frac{\partial \mathbf{u}_0}{\partial z} \right)^2 \right]^{1/2}$$

$$= \tau_0 + \beta\tau_1 + \beta\tau', \tag{36}$$

where τ_0, τ_1 and τ' are defined according to (23). Their explicit expressions read:

$$\tau_0 = \rho A_{\mathrm{v}0} \left| \left| \frac{\partial \mathbf{u}_0}{\partial z} \right| \right|, \quad \tau_1 = \rho A_{\mathrm{v}0} \hat{\boldsymbol{\tau}}_0 \cdot \frac{\partial \mathbf{u}_1}{\partial z},$$
$$\tau' A_{\mathrm{v}0} \hat{\boldsymbol{\tau}}_0 \cdot \frac{\partial \mathbf{u}'}{\partial z} + \rho A'_\mathrm{v}(y) \left| \left| \frac{\partial \mathbf{u}_0}{\partial z} \right| \right|, , \tag{37}$$

respectively, where $\hat{\boldsymbol{\tau}}_0$ denotes the instantaneous unit vector of the bottom stress vector $\boldsymbol{\tau}_0$. To determine the tidal constituents of τ', one can use the fact that $\mathbf{u}'$ contains M_0, M_2 and M_4 while $\hat{\boldsymbol{\tau}}_0$ contains only M_2 and its odd overtides.

[49] The induced sediment field is forced, due to the bottom shear stress, at M_0 and even overtides of M_2 while contributions at M_2 and odd overtides thereof are excited through the advection terms in (33). Thus, the M_2 component of the induced sediment field is generated indirectly so that we expect this constituent to be weak compared to the induced M_0 and M_4 components.

[50] From equations (33)–(35) and (37) it is found that c' and τ' can be written in a similar way as the induced fluid variables, namely:

$$Q = \frac{h(y)}{H} F_Q(z,t) + \frac{\mathrm{d}h}{\mathrm{d}y} G_Q(z,t). \tag{38}$$

Here, Q is either c' or τ' The function F_Q contains frequency contributions at M_0 and even multiples of the basic frequency (M_4, M_8, etc.) while G_Q only has contributions at M_2 and its odd overtides. Once again, for each tidal component the lateral dependence separates out, so that the induced sediment concentration can be solved in a similar fashion as the induced water motion.

4.3.3. Equilibrium Bottom Tilt

[51] The net lateral sediment mass flux per unit width $\mathcal{F}$ reads:

$$\mathcal{F} = H \left[\langle \overline{vc} \rangle - K_\mathrm{h} \frac{\partial \langle \overline{c} \rangle}{\partial y} \right]$$
$$= \beta H \left[\langle \overline{v_0 c_1} + \overline{v_1 c_0} \rangle + \langle \overline{v_0 c'} + \overline{v' c_0} \rangle - K_\mathrm{h} \frac{\partial \langle \overline{c'} \rangle}{\partial y} \right]$$
$$= \beta [\mathcal{F}_0 + \lambda \mathcal{F}'], \tag{39}$$

where $\mathcal{F}_0 = H\langle \overline{v_1 c_1} + \overline{v_1 c_0} \rangle$ is the nonzero flux induced by the external tide moving over the horizontal bottom: it contains the phase difference φ between the depth-averaged M_2 tidal velocity $\bar{u}_0 = U\cos(\sigma t)$ and the M_4 component $\bar{u}_1 = \beta U \cos(2\sigma t - \varphi)$. The term $\lambda\mathcal{F}'$ gives the correction to this depth-integrated flux due to the tilting bottom. Here $\mathcal{F}'$ is a flux which is independent of the bottom tilt and can be computed from the equations just discussed. From (39), the equilibrium bottom tilt ($\mathcal{F} = 0$) is found as:

$$\lambda = -\frac{\mathcal{F}_0}{\mathcal{F}'}. \tag{40}$$

Finally we wish to remark that the a priori assumption of the bottom profile (22) with a constant slope in the lateral

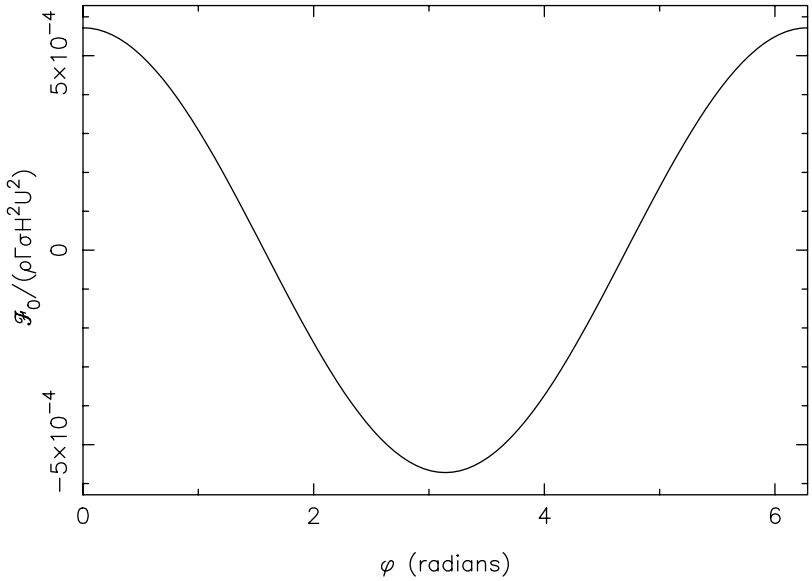

Figure 4. The depth-integrated lateral sediment flux $\mathcal{F}_0$ (in units $\rho\Gamma\sigma H^2U^2 \sim 15$ kg m^{-1} s^{-1}) as a function of phase difference φ between the external M_2 and M_4 tide.

direction results in a self-consistent solution of the model, hence its choice is justified a posteriori.

5. Results

5.1. Net Mass Flux Per Unit Width $\mathcal{F}_0$

[52] It appears from the analysis of section 4 that the equilibrium bottom will have a lateral tilt in case that the net sediment mass flux per unit width $\mathcal{F}_0$ in equation (39) is nonzero. As can be seen from its definition this quantity is due to an asymmetrical external tidal current (M_2 + M_4) moving over a horizontal bottom. Therefore we first show in Figure 4 the dependence of $\mathcal{F}_0$ on the phase difference between the external M_2 and M_4 current. Here the default parameter values for the WS estuary have been taken, see Table 3. The values on the vertical axis are scaled with $\Gamma\rho\sigma H^2U^2$ so that the maximum value of $\mathcal{F}_0$ approximately equals 7×10^{-3} kg m^{-1} s^{-1}. Thus the total sediment flux per unit width $\beta\mathcal{F}_0$ is of the order of 10^{-3} kg m^{-1} s^{-1}.

[53] Note that $\mathcal{F}_0$ varies proportional to $\cos\varphi$. It means that for strong flood (ebb)-dominated currents, i.e., $\varphi = 0$ ($\varphi = \pi$) there will be a net advective flux of sediment to the left (right) when viewing in the flood direction. There are also two cases ($\varphi \sim \pi/2$ and $\varphi \sim 3\pi/2$) for which $\mathcal{F}_0 = 0$, such that the equilibrium bottom will be horizontal. This behavior can be understood from the fact that the time dependence of the currents and concentration are close to those of the external tides and of the bottom stress, respectively. This can be seen in Figures 5 and 6. The first shows all four components of the externally imposed M_2 tide; clearly the along-channel directed $\cos(\sigma t)$-component dominates over the other three contributions. Figure 6 shows the spatial and temporal variation of the sediment concentration. It appears that the settling lag timescale is approximately 450 s, which is much smaller than the tidal period. Thus the sediment concentration is almost in phase with the bottom stress. Note also that the typical e-folding depth of the sediment concentration profile agrees well with the theoretical estimate $K_v/w_s = 0.4H$.

[54] The time behavior of velocity, stress and sediment concentration are thus approximately given by (see equation (37); note that Figure 5 implies $\hat{\tau}_0 \approx \mathrm{sg}(\cos(\sigma))$):

$$(u_0, v_0) \propto \cos(\sigma t), \tag{41}$$

$$(u_1, v_1) \propto \cos(2\sigma t - \varphi), \tag{42}$$

$$(\tau_0, c_0) \propto |\cos(\sigma t)|, \tag{43}$$

$$(\tau_1, c_1) \propto \mathrm{sg}(\cos(\sigma t))\ \cos(2\sigma t - \varphi). \tag{44}$$

From these expressions it follows that:

$$\langle v_0 c_1 \rangle \propto \int_0^P |\ \cos(t)|\ \cos(2t - \varphi)\mathrm{d}t \propto \cos(\varphi), \tag{45}$$

and similarly for $\langle v_1 c_0 \rangle$, so that $\mathcal{F}_0\ (\varphi) = \langle \overline{v_0 c_1} + \overline{v_0 c_1} \rangle \propto \cos\ (\varphi)$. Note that this qualitative result is firm in that it is independent of the precise prescription of model parameters: only the approximate validity of assumptions (41)–(44) is required.

5.2. Net Mass Flux Per Unit Width $\mathcal{F}'$ and Lateral Bottom Tilt

[55] Equation (39) shows that, in order to maintain morphodynamic equilibrium, the net mass flux $\mathcal{F}_0$ has to be compensated by a net mass flux $\lambda\mathcal{F}'$. Besides the fact that $\mathcal{F}'$ is independent of bottom tilt λ, as was explained in section 4.3.3, this term is also independent of the phase difference φ between the external M_2 and M_4 current. This is because the induced flow and sediment problem only involve the external M_2 tide.

[56] Note that $\mathcal{F}'$, according to its definition in equation (39), consists of two advective contributions and a dispersive part. The model results for the default case indicate that

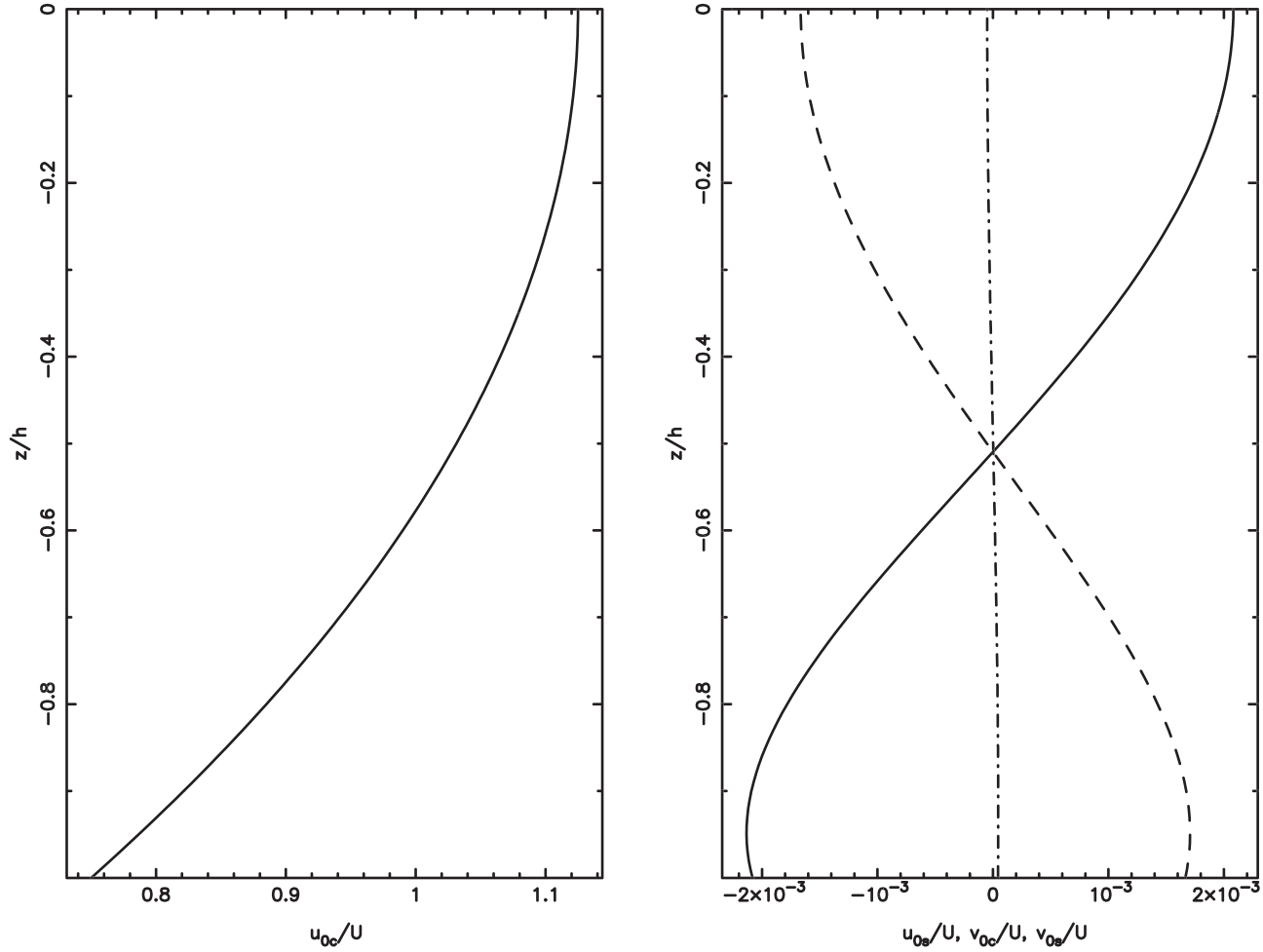

Figure 5. Left: vertical profile of the along-channel directed external M_2 flow that varies $\propto \cos(\sigma t)$. Right, the other external M_2 components: along-channel, $\propto \sin(\sigma t)$ (solid) and cross-channel $\propto \cos(\sigma t)$ (dashed) and $\propto \sin(\sigma t)$ (dash–dot–dash).

the latter term always dominates over the first two terms (by six orders of magnitudes). Large ratios of dispersive and advective contributions were also found if the friction parameters A_{v0} and s_0 were varied by two orders of magnitude. Hence $\mathcal{F}'$ is governed mainly by lateral dispersion which in turn depends solely on the depth-integrated induced residual sediment concentration $H\langle\overline{c'}\rangle$. The value of $\mathcal{F}'$ for the WS default case is -0.044 kg m^{-1} s^{-1}.

[57] Since $\mathcal{F}'$ turns out to be negative it implies that a positive (negative) bottom tilt λ is related with a depth-integrated concentration gradient in the positive (negative) y-direction. This is also clear from Figure 7 which shows that in case of a flood (ebb)-dominated flows, i.e., $\varphi = 0$ ($\varphi = \pi$), the lateral bottom tilt λ is positive (negative) and hence the shallowest depths and the largest concentrations appear on the left (right) when viewing in the flood direction. Thus the model indicates that the depth-integrated sediment concentration increases toward shallower water. The physical explanation for this will be given in the next subsection.

[58] Figure 7 shows that the maximum tilt λ_{max} found for the default case is $\lambda_{max} \approx 0.16$. For the WS estuary (width of 5 km) this corresponds to a depth difference of approximately 30 cm between the two channel sidewalls. However, since the flux $\mathcal{F}'$ is proportional to the lateral dispersion coefficient K_h, it is clear that the values of the tilt scale with K_h^{-1}. As lateral dispersion coefficients may be much lower than the default value, larger depth differences (up to meters) may occur in real estuaries.

[59] Finally, we briefly mention typical maximum values for the tilt that occur when A_{v0} and s_0 are varied (keeping all other parameters in Table 3 fixed). For realistic stress parameter values ($s_0 > 10^{-3}$ ms^{-1}), its typical magnitude is in the range 0.2–0.4 for $A_{v0} < 0.07$ m^2 s^{-1} while $\lambda_{max} \approx 0.1$ if 0.07 m^2 s^{-1} $< A_{v0} <$ 0.14 m^2 s^{-1}. For low values of the friction parameters ($s_0 < 10^{-3}$ ms^{-1}, $A_{v0} < 0.01$ m^2 s^{-1}), λ_{max} decreases linearly with A_{v0} and s_0.

5.3. Physical Interpretation of the Induced Sediment Flux

5.3.1. Induced Residual Bed Shear Stress

[60] Here we will explain one of the important results of section 5.2, viz. that the mean sediment concentration $\langle c' \rangle$ increases toward shallower water. From section 4.3.2 we see that $\langle c' \rangle$ is generated by the residual component of boundary conditions (34) and (35) since advective terms are absent from the M_0 component of (33). In this generation, the

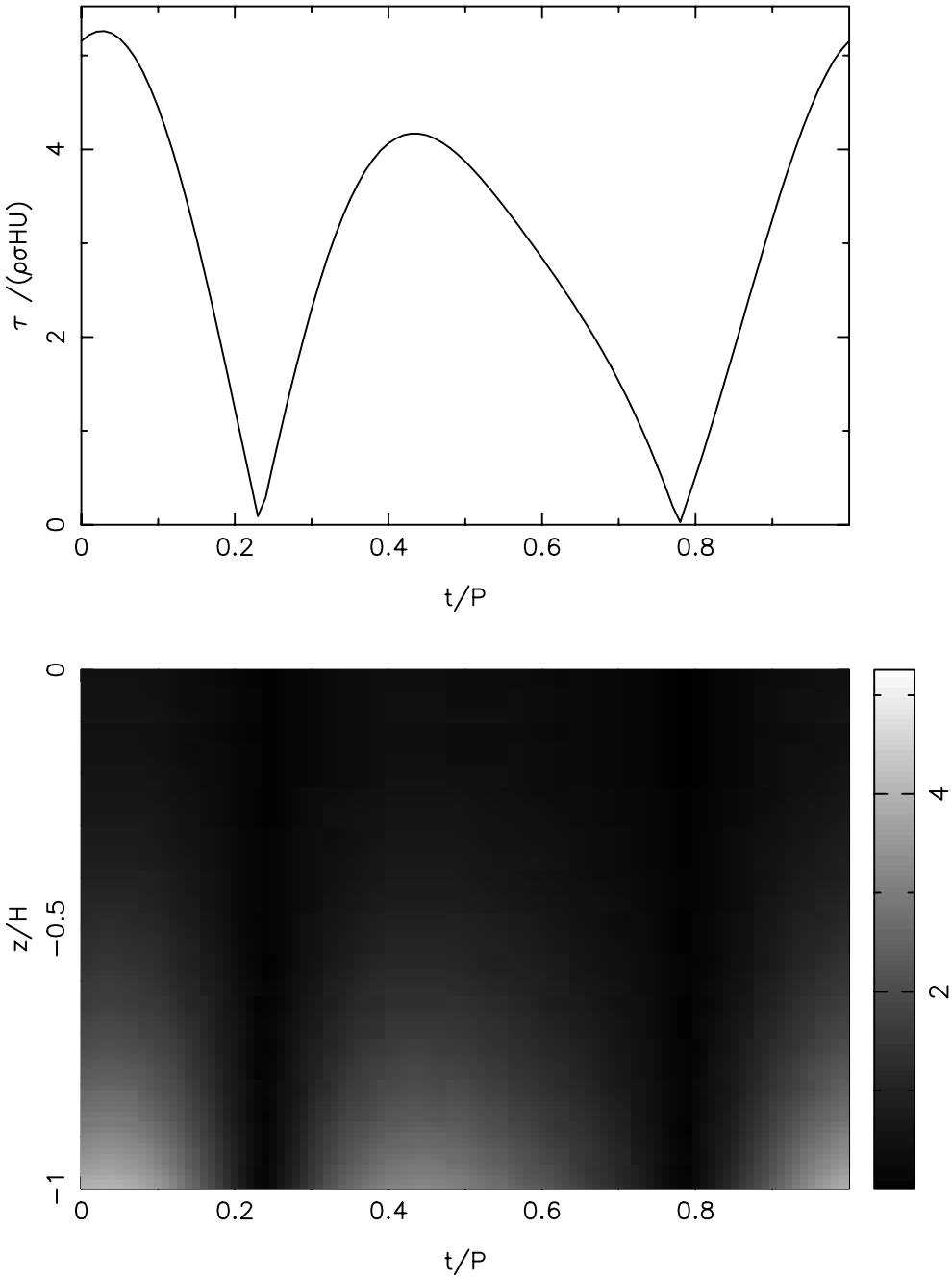

Figure 6. Top: bed shear stress magnitude throughout a tidal period P. Bottom: dimensionless sediment concentration profile as a function of time. Here, concentration and stress have been scaled in units $\rho\sigma UH\Gamma \sim 1.5$ kg m^{-3} and $\rho\sigma HU \sim 1.4$ N m^{-2}, respectively.

induced water motion influences the erosion of induced sediment through $\langle\tau'\rangle$ (r.h.s. of equation (35)) for which the M_2 component of the induced water motion is important. The latter can be understood from expression (37) where it is recalled that the induced tidal flow has no spectral contributions above M_4. For depth-independent friction parameters ($m = n = 0$, i.e., $A_v' = s' = 0$) this is immediately clear from (37) which then gives:

$$\langle\tau'\rangle = \langle\hat{\boldsymbol{\tau}}_0 \cdot A_{v0}\frac{\partial \mathbf{u}'}{\partial z}\rangle \approx \langle \mathrm{sg}(\cos(\sigma t))A_{v0}\hat{\mathbf{x}} \cdot \frac{\partial \mathbf{u}'}{\partial z}\rangle = \frac{2A_{v0}}{\pi}\frac{\partial u_c'}{\partial z}. \quad (38)$$

Consequently, we find that the induced residual stress $\langle\tau'\rangle$ is governed by u_c' (which is the cosine component of the M_2 part of u').

[61] Figure 8 shows the vertical variation of u_c' near the sidewall above a shoal ($h(y) > 0$). For depth-independent friction parameters A_v and s (left panel) we find $u_c' < 0$, i.e., the flow is decelerated above the shoal. This is in agreement with the increase of bottom friction as water depth decreases. The vertical derivative of u_c', however, is *positive* so that the residual bed shear stress $\langle\tau'\rangle$ is found to increase above shallow regions.

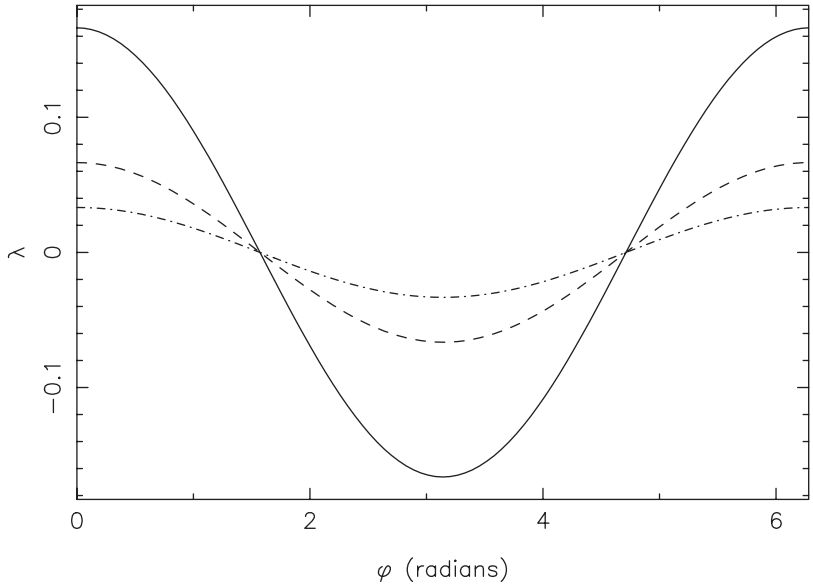

Figure 7. Lateral bottom tilt λ versus phase difference φ between external M_2 and M_4 tide. The different curves refer to different values of ithe lateral diffusion coefficient: $K_h = 20$ m^2 s^{-1} (solid line), $K_h = 50$ m^2 s^{-1} (dashed) and $K_h = 100$ m^2 s^{-1} (dash−dot−dash).

[62] Now consider the effect of depth-dependent friction parameters on the induced M_2 flow. This is displayed in the right panel of Figure 8 for flow near the sidewall above a shoal. It turns out that the induced residual bottom stress, as given by equation (37), is nearly unaltered so that depth dependence of the friction parameters does not seem to affect the residual bottom shear stress $\langle\tau'\rangle$.

5.3.2. Induced Residual Concentration

[63] Next we will discuss the induced residual sediment concentration. We first focus on its bottom value, hereafter referred to as $\langle c_b'\rangle$. Its value is obtained by using the alternative expression $\langle S_\star\rangle = 0$ for morphodynamic equilibrium (see remarks below equation (17). Using definitions (15), (22) and the assumption of a weak overtide ($\beta \ll 1$) this condition can be rewritten into the following expression for $\langle c_b'\rangle$:

$$\langle c_b'\rangle = \Gamma\langle\tau'\rangle + h(y)\left[\Gamma\frac{\partial\langle\tau_0\rangle}{\partial z} - \frac{\partial\langle c_0\rangle}{\partial z}\right], \qquad (46)$$

where all quantities are understood to be evaluated at $z = -H$. Let us again consider the situation above a shoal ($h(y) > 0$). In that case, we already saw in section 5.3.1 that $\langle\tau'\rangle$ will have a positive value that is unaffected by depth-dependence of A_v and s. As a consequence, $\langle c_b'\rangle$ will not be sensitive to such depth-dependence either. The term between square brackets in (46) gives the change in the erosion-deposition function as the bed level is increased. It contains contributions from vertical variation of sediment erosion (τ_0) and settling (c_0) which yield negative and positive contributions to $\langle c_b'\rangle$, respectively. For thin sediment layers (thickness less than the water depth H), the settling effect dominates over the effect of erosion so that the second contribution to (46) is positive. This is the case for the default WS case where the sediment layer thickness is approximately 0.4 H (see Figure 6).

[64] Figure 9 shows the vertical variation of $\langle c'\rangle$. The dashed line corresponds to depth independent friction parameters and gives a simple exponential decay with height. The solid line refers to $n = m = 1$: it is clearly seen that $\langle c'\rangle$ is decreased throughout the water column. This is due to the decrease of vertical turbulent diffusion K_v above a shoal (recall that $K_v = A_v$) so that downward-directed sediment settling will become relatively more important. The latter effect leads to a decrease in induced residual concentration. For the WS parameter settings, though, the depth-integrated induced concentration $H\langle\bar{c}'\rangle$ is still positive above shoals. Using the above arguments one finds similarly that $H\langle\bar{c}'\rangle$ is negative in deep parts ($h(y) < 0$) of the channel. As a result, the induced flux $\mathcal{F}'$ will flow from shallow to deep regions.

5.4. Application to Field Data

[65] Our model results show that that the lateral bottom tilt varies as cos φ, with φ the phase difference between horizontal M_2 and M_4 tide. In order to gain some support for this from field data, one should analyze bathymetric data from a long, straight estuary with a width of at least a tidal excursion length. In that case, the variation of φ along the estuary can be plotted against the lateral bottom variation.

[66] For the reference system that is considered in this paper (the WS, see Figure 10), this analysis is not straightforward because of several reasons. First, near the inlet the estuary is relatively straight, but φ is close to $-\pi/2$ there. Hence λ is effectively zero in this part of the estuary. Further inward, φ increases but at approximately 50 km from the inlet, the channel becomes very narrow: in this region, the Rossby number is large so that Coriolis effects will be difficult to detect. Hence, only at the middle part of the estuary, both phase difference and channel width appear to be acceptable to check the model: this region has been displayed explicitly in Figure 10. This part of the WS consists of two distinct meanders; these will be referred to hereafter as

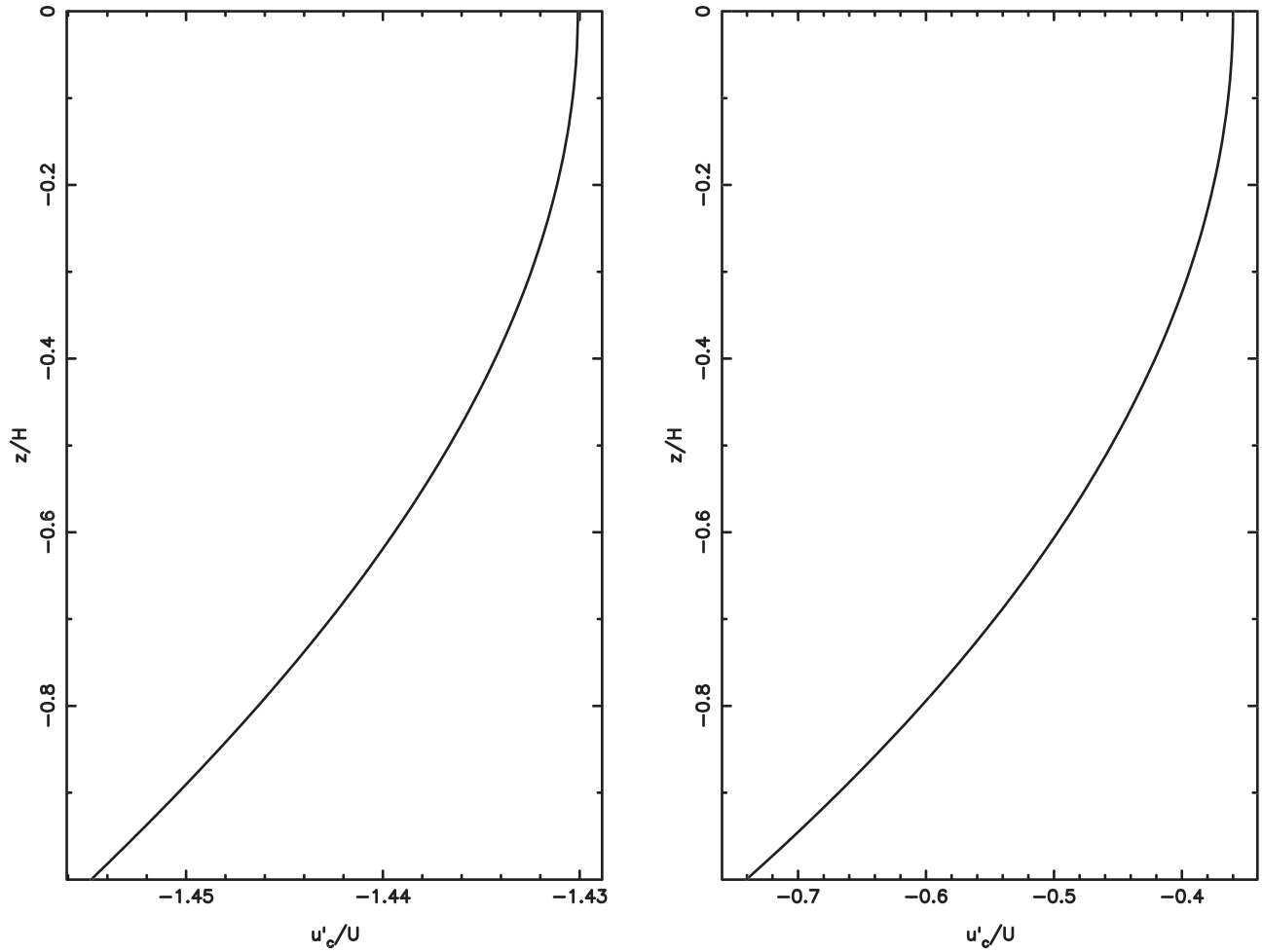

Figure 8. Induced M_2 component of the along-channel flow, time dependence $\propto \cos(\sigma t)$. The left panel shows the vertical profile for depth independent friction parameters A_{v0} and s_0 while the right panel refers to the depth dependent case ($n = m = 1$).

"Curve 1" and "Curve 2", respectively (see Figure 10). As is well known [*Kalkwijk and de Vriend*, 1980], such meanders exhibit lateral variation of bottom depth due to secondary circulations that arise from flows around a bend. In terms of the model presented in the paper, such variations are $O(1)$ while the Coriolis effect is $O(\beta)$. Hence it would be difficult to filter out the latter effect from field data.

[67] Given these restrictions, we have investigated the presence of an asymmetry in the cross-sectional bottom variation of the meanders. Such an asymmetry may be related to the Coriolis effect as follows. In the region of interest, φ varies from -1.4 to -1.1 which implies that λ is expected to be positive (southern part deeper than the northern part). Curvature effects, on the other hand, cause the bathymetry to be deep near outer bends and shallow near inner bends. Hence for Curve 1, the curvature effect would yield larger depths near southern banks than near northern banks. The reverse holds for Curve 2. As a result, it is thus expected that the Coriolis effect would enhance the lateral depth difference in Curve 1, while it would weaken the depth difference across Curve 2. We are interested in a lateral bottom profile on a channel-wide scale while the bathymetry is dominated by a complex small-scale channel-shoal system (see Figure 10). In order to abstract a linear bottom profile from this complex morphology, we proceeded along the following lines. First, we observe that there are two pronounced tidal channels in Curves 1 and 2. Next, we made several (150–200) cross-channel slices in which these channels show up as pronounced troughs. Cross-channel location and depth of these two troughs were used to define the lateral bottom profile as given by (22); this yields representative values for H and λ. The values for λ thus obtained read:

$$\lambda = 7.22 \pm 6.67 \text{ for Curve 1},$$

$$\lambda = -3.98 \pm 2.04 \text{ for Curve 2}.$$

Quantitatively, this result cannot be compared to the model presented in this paper as the value for lateral dispersion is not well known (K_h may vary from 0.1 $m^2\ s^{-1}$ to several tens $m^2\ s^{-1}$). Qualitatively, though, our findings support the expectation that the lateral tilt in Curve 1 is more pronounced than in Curve 2.

6. Discussion

6.1. Lateral Sediment Balance

[68] A few aspects of the model results deserve some discussion. First it has been assumed that in equilibrium the

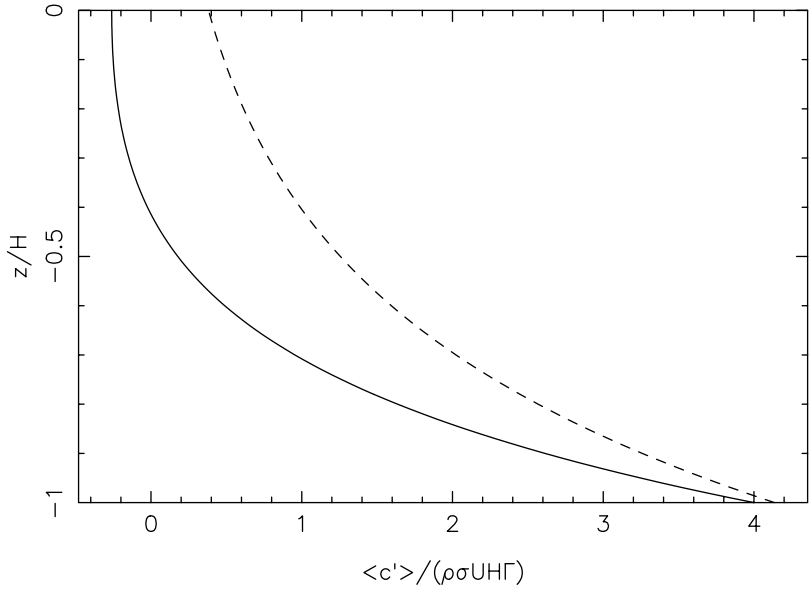

Figure 9. Vertical variation of the induced residual concentration at the shallow side near the bank. Solid: depth dependent friction parameters ($n = m = 1$), dashed: profile for $n = m = 0$ (no depth dependence in A_v or s).

net lateral sediment mass flux per unit width $\mathcal{F}_0$ is compensated by a lateral dispersive flux $\lambda\mathcal{F}'$. Alternatively, one could consider the possibility of gravitational bedslope effects balancing the flux $\mathcal{F}_0$. A typical magnitude for the resulting bedslope flux $\mathcal{F}_{\text{bed}}$ is given by

$$\mathcal{F} = -\rho - s(1-p)\alpha\langle \| \mathbf{u}(-H,t) \|^3\rangle\mu\frac{\partial z_b}{\partial y}$$
$$\approx \beta\rho_s(1_p)\alpha\langle \| \mathbf{u}_0(_H,t) \|^3\rangle\mu\lambda\frac{H}{B},$$

where (22) was used in the final step. Typical values for α and μ are $\alpha = 10^{-5}$ s^2 m^{-1} and $\mu = 1$, see *Dyer* [1986]. For the default WS parameter values, $\mathcal{F}_{\text{bed}}/\mathcal{F}' \approx O(10^{-3})$ so that bedslope effects are found to be too small to establish the lateral tilt.

[69] Another remarkable aspect of the present model is that, for typical WS parameter values, it yields a dispersive flux which is directed from shallow to deep regions. This is opposite to dispersive fluxes in 2DH models, at least when the latter models assume depth-independent erosion and deposition of sediment [*Schuttelaars and de Swart*, 1999]. In that case, lower sediment concentrations are found above shallow parts because the sediment-pickup function is related to the depth-averaged velocity, which decreases above shoals due to increased friction. The dispersive flux in the present model acts differently for two reasons. First, the bed shear stress is related to the vertical derivative of horizontal

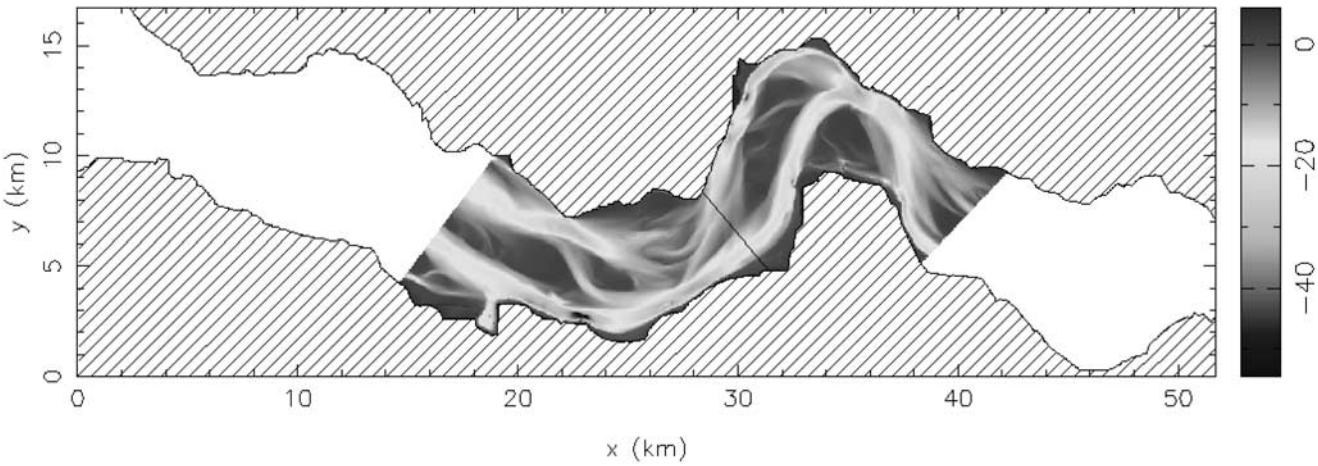

Figure 10. Central marine part of the WS estuary. The northward direction is at the top of the figure while the seaward side is to the left. For the region considered in this paper, the bathymetry is shown as an image plot (unit: meters). The cross-sectional line in this part marks the division between the two meanders that constitute the region of interest: the western and eastern bend are referred to as "Curve 1" and "Curve 2", respectively. See the text for further explanation.

velocity at the bottom rather than the depth-averaged velocity. Second, the residual concentration is largely determined by near-bed changes in erosion-deposition fluxes as the bed is raised or lowered. These effects explicitly require information on the vertical variation of velocity and sediment concentration near the bottom and are thus not incorporated in a 2DH formulation. As a result the present model gives higher residual concentrations above shoals, at least when the sediment layer is thinner than the water depth.

6.2. Validation of the Model

[70] In contrast to its robust qualitative features, accurate quantitative estimates for the lateral bottom tilt λ appear to be problematic. This is mainly due to the dependence of λ on the lateral coefficient of diffusion K_h, the size of which is not well known. Estimates from field data and laboratory experiments indicate that realistic values of K_h vary from 0.1 $m^2\ s^{-1}$ to several tens $m^2\ s^{-1}$ [e.g., *Fischer et al.*, 1979, section 7.3.2]. For the default value $K_h = 20\ m^2\ s^{-1}$ adopted in this paper, the lateral bottom tilt was found to yield a cross-sectional depth difference of a few percent (typically a few decimeters). However, as lateral diffusion may be an order of magnitude smaller, a more noticeable depth difference (up to several meters) may occur in reality since $\lambda \propto 1/K_h$. Thus it appears that the lateral bottom tilt itself should be detectable from field data, at least in principle.

[71] As to qualitative features, it is evident that more effort has to be put in confirming the firm predictions that have been presented in this paper. In particular, a validation of the abovementioned cos φ dependence for the lateral tilt should be confronted against data from a relatively straight, effectively nonmeandering tidal channel. Moreover, this channel must have sufficient length in order to guarantee a relevant variation of φ along the embayment. As was pointed out in section 5.4, the WS estuary does not qualify for such a thorough analysis since it shows meandering behavior.

[72] A different way to test the tilting bottom model may be obtained from estuaries with a significant residual throughflow (river discharge) rather than an M_4 overtide. In that case, there is no phase difference φ so that only information about the sign and magnitude of λ may be obtained. Fortunately, though, several such estuaries appear to be relatively straight over a large portion of their length (e.g., James River estuary [*Valle-Levinson et al.*, 2000]) so that disturbing effects of meandering are circumvented. Contrary to the WS, however, estuaries with significant river discharges are usually not well-mixed so that vertical mixing of momentum and sediment is affected by effects of partial stratification. The present model can be straightforwardly extended to include such effects [see *Van Kreeke and Zimmerman*, 1988; *Friedrichs and Hamrick*, 1996].

6.3. Relevance for Modeling of Bathymetric Features

[73] From the viewpoint of idealized modeling, a nonhorizontal equilibrium bottom may serve as a nontrivial starting point for the study of bottom pattern formation as an inherent instability mechanism. It represents a relevant extension of the model by *Seminara and Tubino* [1998] who considered a horizontal basic state. Several new results are expected due to the combined presence of Coriolis force and overtides. For instance, Coriolis effects will modify the behavior of ebb and flood dominated tidal channels. Thresholds occur on smaller scales (up to a kilometer) and will not be influenced directly by Coriolis effects. Overtides, however, are still expected to play an important role in these regions. Finally, an interesting question is to what extent Coriolis effects may still play an indirect role in threshold dynamics since thresholds are strongly linked with the meandering behavior of tidal channels.

7. Conclusions

[74] In this paper, new results have been presented regarding the combined effect of Coriolis force and external overtides on bottom patterns that constitute a morphodynamic equilibrium. Such equilibrium configurations should be interpreted as a global bathymetry that varies on the scale of the embayment width. Hence they are the mean bed profiles that underlie the complex channel/shoal bathymetry that occur on smaller length scales.

[75] The equilibrium bed profile is horizontal if only a single external tidal mode is imposed or Coriolis effects are absent. If external overtides and Coriolis force are simultaneously present, a net lateral sediment flux exists which requires a cross-channel variation of the bottom in order to maintain morphodynamic equilibrium. For the case of an external M_4 overtide it appears that such an equilibrium is characterized by a linear lateral bottom profile which has its shallow part to the left (right) for flood (ebb) dominated external tidal forcing. Moreover, the tilt of the lateral profile varies $\propto \cos(\varphi)$. These results are mostly robust, i.e., independent of the precise parameterization of viscosity and diffusion: they only require a bed shear stress that depends upon the magnitude of velocity and a settling time that is short compared to a tidal period. It should be emphasized that the lateral bottom variation is a genuine 3D-effect as it is a consequence of lateral circulations that are absent in a vertically averaged model (see section 4.1). The lateral tilt is predominantly maintained by dispersive sediment fluxes rather than by advective processes or gravitational bedslope effects. As a result, the value of the slope is inversely proportional to the lateral coefficient of dispersion K_h. Depending on the value of the latter parameter, the cross-channel variation of the water depth may be of the order of meters.

[76] **Acknowledgments.** The authors are indebted to the National Institute for Coastal and Marine Management (RIKZ) at Middelburg, Netherlands, for the availability of the Western Scheldt data. This research is supported by the RIKZ at The Hague and through grant no. 810.33.003 of the Netherlands Organisation for Scientific Research (NWO). Also, the authors wish to thank Henk Schuttelaars as well as C. T. Friedrichs and the other two (anonymous) referees for their helpful comments on the submitted manuscript.

References

Davies, A. G., and C. Villaret, Eulerian drift induced by progressive waves above rippled and very rough beds, *J. Geophys. Res.*, *104*, 1465–1488, 1999.

De Jong, K., and A. W. Heemink, A model for long-term morphodynamic behaviour of tidal basins, long estuaries, and tidal rivers, *Tech. Rep. 96-153*, Delft Univ. of Technol., Delft, Netherlands, 1996.

De Vriend, H. J., Mathematical modelling of meso-tidal barrier island coasts, 1, Empirical and semi-empirical models, in *Advances in Coastal and Ocean Engineering*, edited by P.-F. Liu, pp. 115–149, World Sci., River Edge, N. J., 1996.

Dyer, K. R., *Coastal and Estuarine Sediment Dynamics*, John Wiley, New York, 1986.

Fischer, H. B., E. J. List, R. C. Y. Koh, J. Imberger, and N. H. Brooks, *Mixing in Inland and Coastal Waters*, Academic, San Diego, Calif., 1979.

Friedrichs, C. T., and D. G. Aubrey, Tidal propagation in strongly convergent channels, *J. Geophys. Res.*, *99*, 3321–3336, 1994.

Friedrichs, C. T., and J. H. Hamrick, Effects of channel geometry on cross sectional variation in along channel velocity in partially stratified estuaries, in *Buoyancy Effects on Coastal and Estuarine Dynamics*, edited by D. Aubrey and C. Friedrichs, pp. 283–300, AGU, Washington, D. C., 1996.

Friedrichs, C. T., and O. S. Madsen, Nonlinear diffusion of the tidal signal in frictionally-dominated embayments, *J. Geophys. Res.*, *97*, 5637–5650, 1992.

Jeuken, C. J. L., On the morphodynamic behaviour of tidal channels in the westerschelde estuary, Ph.D. thesis, Univ. of Utrecht, The Netherlands, 2000.

Kalkwijk, J. P. T., and H. J. de Vriend, Computation of the flow in shallow river bends, *J. Hydraul. Res.*, *18*(4), 327–342, 1980.

Lanzoni, S., and G. Seminara, On tide propagation in convergent estuaries, *J. Geophys. Res.*, *103*, 30,793–30,812, 1998.

Maas, L. R. M., and J. J. M. van Haren, Observations on the vertical structure of tidal and inertial currents in the central north sea, *J. Mar. Res.*, *45*, 293–318, 1987.

Prandle, D., The vertical structure of tidal currents and other oscillatory flows, *Cont. Shelf Res.*, *1*(2), 191–207, 1982.

Rozovskii, I. L., Flow of water in bends of open channels, Israel Progr. for Sci. Trans., Jerusalem, 1961.

Schuttelaars, H. M., and H. E. De Swart, An idealized long-term morphodynamic model of a tidal embayment, *Eur. J. Mech. B, Fluids*, *15*, 55–80, 1996.

Schuttelaars, H. M., and H. E. de Swart, Initial formation of channels and shoals in short tidal embayments, *J. Fluid Mech.*, *386*, 15–42, 1999.

Schuttelaars, H. M., and H. E. de Swart, Multiple morphodynamic equilibria in tidal embayments, *J. Geophys. Res.*, *105*, 24,105–24,118, 2000.

Seminara, G., and M. Tubino, On the formation of estuarine free bars, in *Physics of Estuaries and Coastal Seas*, PECS 96, edited by J. Dronkers and M. Scheffers, pp. 345–353, Balkema, Rotterdam, 1998.

Speer, P. E., and D. G. Aubrey, A study of nonlinear tidal propagation in shallow inlet/estuarine systems, 2, Theory, *Estuarine Coastal Shelf Sci.*, *21*, 207–224, 1985.

Valle-Levinson, A., K.-C. Wong, and K. M. M. Lwiza, Fortnightly variability in the transverse dynamics of a coastal plain estuary, *J. Geophys. Res.*, *105*, 3413–3424, 2000.

Van de Kreeke, J., Adaptation of the frisian inlet to a reduction in basin area with special reference to the cross-sectional area of the inlet channel, in *Physics of Estuaries and Coastal Seas*, PECS 96, edited by J. Dronkers and M. Scheffers, pp. 355–362, Balkema, Rotterdam, 1998.

Van de Kreeke, J., and J. T. F. Zimmerman, Gravitational circulation in well ans partially mixed estuaries, in *Physical Processes in Estuaries*, edited by J. Dronkers and W. van Leussen, pp. 495–521, Springer-Verlag, New York, 1988.

Van den Berg, J. H., C. J. L. Jeuken, and A. J. F. van der Spek, Hydraulic processes affecting the morphology and evolution of westerschelde estuary, in *Estuarine Shores: Evolution, Environments and Human Alterations*, edited by K. Nordstrom and C. Roman, pp. 157–184, John Wiley, New York, 1990.

Van Leeuwen, S. M., H. M. Schuttelaars, and H. E. de Swart, Tidal and morphological properties of embayments: Effects of sediment deposition processes and length variation, *Phys. Chem. Earth, Part B, 4*, 365–368, 2000.

Van Rijn, L. C., Sediment transport, 2, Suspended load transport, *J. Hydraul. Eng.*, *110*, 1613–1641, 1984.

Verbeek, H., Z. B. Wang, and P. M. C. Thoolen, Secondary currents in estuarine morphodynamic modelling, a case-study of the western scheldt, paper presented at IAHR Symposium on River, Coastal and Estuarine Morphodynamics, Univ. of Genoa, Genoa, Italy, 1999.

Vreugdenhil, C. B., *Numerical Methods for Shallow Water Flow*, Kluwer, Norwell, Mass., 1994.

Wang, Z. B., T. Louters, and H. J. De Vriend, Morphodynamic modelling for a tidal inlet in the wadden sea, *Mar. Geol.*, *126*, 289–300, 1995.

Wiberg, P. L., A theoretical investigation of boundary layer flow and bottom shear stress for smooth, transitional, and rough flow under waves, *J. Geophys. Res.*, *100*, 22,667–22,680, 1995.

G. P. Schramkowski and H. E. de Swart, Institute for Marine and Atmospheric Research, Utrecht University, P.O. Box 80.005, 3508 TA Utrecht, The Netherlands. (G.P.Schramkowski@phys.uu.nl; H.E.deSwart@phys.uu.nl)